ADVANCED OPTICAL MATERIALS
www.advopticalmat.de

Orientation-Dependent Photoion Emission from Aerosolized Nanostructures

Xu Han, Hao Huang, Xiang Huang, Wei Cao, Qingbin Zhang, and Peixiang Lu**

The laser-irradiated aerosolized nanostructures with complex geometries offer unique opportunities to steer orientation-dependent photoion emission for multiple applications of directional ion sources and photocatalysis. The orientation-dependent photoion emission is characterized by measuring the distribution and probability on differently oriented nanostructures. This unique capability is achieved by introducing momentum-to-space orientation discrimination in the single-shot velocity map imaging technique with the aerodynamic lens. The effect of geometry, polarization, and concentration to control the photoion emission from differently oriented nanostructures is introduced for optimizing the potential applications of photoion emission including directional tunable nanoanode and optical sensors. The mechanism behind controlling the photoion emission is visualized by the variations in the regions of high laser intensity inside the nanostructures responding to the orientation, geometry, and polarization. This work represents an advance in characterizing the photoion emission from the randomly oriented aerosolized nanostructures and facilitates the potential for combining with the pump–probe methods to provide an intuitive understanding of their real-time ionization dynamics.

1. Introduction

Characteristic spatial variations of the ionizing radiation belong to the unique properties of nanostructure due to nanoscale structures can locally enhance a laser field.[1–7] The sensitivity of optical excitation on nanoscale geometry provides a new degree of freedom for controlling nanotarget's photoelectron and photoion emission. It thus stimulates emerging applications like high-quality nanocathode (anode), nanobubbles for cancer therapy, and high-efficiency photocatalysis.[3,8–14] The exploitation of these applications depends heavily on direct mechanistic insight and quantification of photofragments generated from nanostructure. However, the experimental diagnosis of photofragments emission inevitably presents sample damage and charge buildup problems.[15,16] These problems can be largely avoided by introducing an aerodynamic lens (ADL), where the sample is constantly refreshed in the particle beam.[17,18]

The particle beam also provides a noninteracting environment, either with the substrate or other particles. An important advance of the particle technique for angle-resolved studies is the straightforward combination with velocity map imaging (VMI), which can rapidly provide comprehensive information about the photofragment angular distribution.[19] For example, Powell and Süßmann et al. have observed that the photoelectron angular distribution for aerosolized nanospheres shows a laser polarization dependence with the combined method.[20–22] It has also been demonstrated that the photofragment angular distribution for nanospheres is sensitive to the type of materials and size.[23,24] The preferred backward emission occurs along the laser propagation direction for the opaque nanospheres, namely nano-shadowing. While if the nanospheres are transparent to the exciting radiation, a nano-focusing effect occurs when the wavelength of the driving laser is similar to or smaller than the size of nanospheres, corresponding to an enhanced forward emission in the direction of laser propagation. The physical essential behind the changes in the photofragment angular distributions is that the photofragments are preferentially formed in regions of high light intensity with a probability determined by the local light intensity.[24] Besides the laser polarization, material, and size of nanospheres, the slight variations in the geometry of more complex nanotarget can also significantly affect the enhancement of the incident laser fields. Unlike nanospheres, the near-field enhancement of complex nanotarget is orientation-dependent.

For a dimer system consisting of two SiO_2 spheres, Finite Difference Time Domain (FDTD) calculations predict that the dimer systems parallel to the laser polarization direction or having a slight deviation from the above orientation condition could represent a donut-shaped enhanced field distribution around the contacting area of the nanospheres.[25,26] Similar orientation-dependent near-field enhancement excites for other nonspherical symmetric nanotargets like nanotubes and

X. Han, X. Huang, W. Cao, Q. Zhang, P. Lu
Wuhan National Laboratory for Optoelectronics and School of Physics
Huazhong University of Science and Technology
Wuhan 430074, P. R. China
E-mail: zhangqingbin@hust.edu.cn; lupeixiang@hust.edu.cn
H. Huang
School of Mechanical Science and Engineering
Huazhong University of Science and Technology
Wuhan 430074, P. R. China
P. Lu
Optics Valley Laboratory
Hubei 430074, P. R. China

The ORCID identification number(s) for the author(s) of this article can be found under https://doi.org/10.1002/adom.202201260.

DOI: 10.1002/adom.202201260

nanocubes.[6,27] However, the investigations on the orientation-dependent photofragment emission for aerosolized nanotargets with complex shapes are still comparatively sparse, not to mention taking advantage of the orientation effect. The challenge lies in the random orientation of ADL transferred samples due to the intense collision between carrier gas molecules and nano samples.[24] The attempt to integrate images of the multi-shot ion emissions will smear the sensitivity of photofragment angular distributions on oriented samples (as shown in the Experimental Section). The orientation characterization of the nanostructure when attempting to control the photofragment emissions from differently oriented nanostructures is crucial, but still lacking.

In this letter, we propose an orientation-binned scheme aimed at studying the photoion emission from ADL-transferred aerosolized nanotargets in multiple orientations while avoiding the average effect. This method is based on correlating the single-shot photoion angular distributions (PIADs) with the orientation of the excited nanotarget in the laboratory coordinate by the molecular dynamics (MD) simulation. This solution allows us to use the ADL which has a widespread transmission window for efficiently transmitting nanotargets with different morphology and orientation. The orientation-dependent photoion emission is characterized in terms of the PIAD and the probability of each specific PIAD. Then we further show how laser polarization, geometry, and concentration affect the photoion emission from the differently oriented nanostructures. When changing the laser polarization, the probabilities of the round and bandlike PIADs vary inversely, indicating the selective excitation of differently oriented nanotubes for directional tunable nanoanode. The PIADs from the face-centered cubic sodium chloride (NaCl) crystals can be fully switched between ringlike and bandlike by only changing the laser polarization, showing the potential to be an optical sensor. And we can regulate the probability of bandlike PIAD from the dimer system by adjusting the concentration. The changes in PIADs and the different trends of the probabilities of specific PIADs are explained by laser field distribution inside the nanostructures for different orientations, geometry, and laser polarization.

2. Orientation-Dependent Photoion Emission

Unlike the nanospheres, the aerosolized nanotube with the cylindrical geometry is suitable for characterizing how the orientation affects photoion emission. Through an ADL, the differently oriented but similar-sized carbon nanotubes (multi-walled, from Aladdin) can be transmitted and then irradiated by a constant laser to exclude the size and polarization effect. Using the single-shot VMI method, different round and bandlike PIADs (**Figure 1**a–d) on the detector plane are observed, which is supposed to result from the variations of the nanotube's orientation.

To understand the relationship between the shape of PIAD and the nanotube's orientation, we explore the spatial variations of the localized plasma on the differently oriented nanotubes, which results in ion emission.[24] Nanoplasma generation is generally described as an avalanche process starting with laser-induced electron ionization.[24,28] The localized plasma will be preferentially formed in regions of high laser intensity (hotspots), indicating the initial position of photoion generation. The field distributions inside the nanotubes with specific orientations are shown in **Figure 2**a,b, simulated by the FDTD calculation. Here the orientation of the nanotube is represented by its axis of symmetry. Inside the nanotube, parallel to the laser polarization, the laser field shows a focusing hotspot (Figure 2a). The strength of the field around the cylindrical surface is stronger than the field around the bottom surfaces to induce more ionization. Inside the nanotube, perpendicular to the laser polarization, the field strength turns out to be almost identical to induce equal ionization everywhere (Figure 2b). It is noticed that the number of atoms around the wider cylinder surface is greater than the number of atoms around the bottom surfaces. Thus, the photoions are primarily generated within the lateral surface regardless of the orientation of the nanotubes. The produced photoions via ionization are sprayed outward due to Coulomb repulsion with each other. However, the photoions emitted toward the undamaged material (two circular end faces of the nanotube) will be absorbed and not be detected. Only the ions emitted outward from the ionized region (surrounding the curved lateral surface) can be recorded. So the three-dimensional (3D) ion emission will show a similar pie shape as the ionized region within the nanotube, which is always homotaxial with the nanotube. To verify this speculation, we simulate the ion emission processes from the differently oriented nanotubes by the MD model.[13,14] The nanotube perpendicular to the detector shows a round simulated PIAD, agreeing well with the projection of the pie-shaped ion emission whose rotation axis of symmetry is perpendicular to the detector. While the nanotube parallel to the detector shows a bandlike simulated PIAD (**Figure 3**a,b), consisting of the projection of the pie-shaped ion emission whose rotation axis of symmetry is parallel to the detector. The simulation establishes the direct correspondence between the shapes of PIADs and the orientations of nanostructures. The detected round (or bandlike) PIAD indicates that the orientation of this nanotube is perpendicular (or parallel) to the detector (**Figure 4**a,b). It provides information about the azimuth angle (Figure 6c, red region) of the nanotube. And for the nanotubes parallel to the detector, the "band" in their bandlike PIADs tends to be orthogonal with the nanotube (Figure 3b). So the elevation angles (Figure 6c, blue region) of the nanotube parallel to the detector can be determined by the orthogonal direction of the "bands" in the bandlike PIADs, as shown by the white regions in Figure 1b–d. The two angles can identify the orientation of the nanotube. This momentum-to-space orientation discrimination is referred to as the orientation-binned method. In principle, the photoelectron angular distribution can also provide similar orientation discrimination. However, due to the increased electron scattering,[24] a lower resolution is expected than that of an ion.

Because the PIAD with a particular shape (specific PIAD) can represent a specific orientation of the nanotubes, the number of times it occurs quantifies how much of the nanotubes with that specific orientation get excited. We manually divide the detected PIADs from the nanotubes into two categories according to their shape characteristics: the round PIADs and the bandlike PIADs. The ellipticity of the shape of PIAD is set as the criterion for classification (see Section S8, Supporting

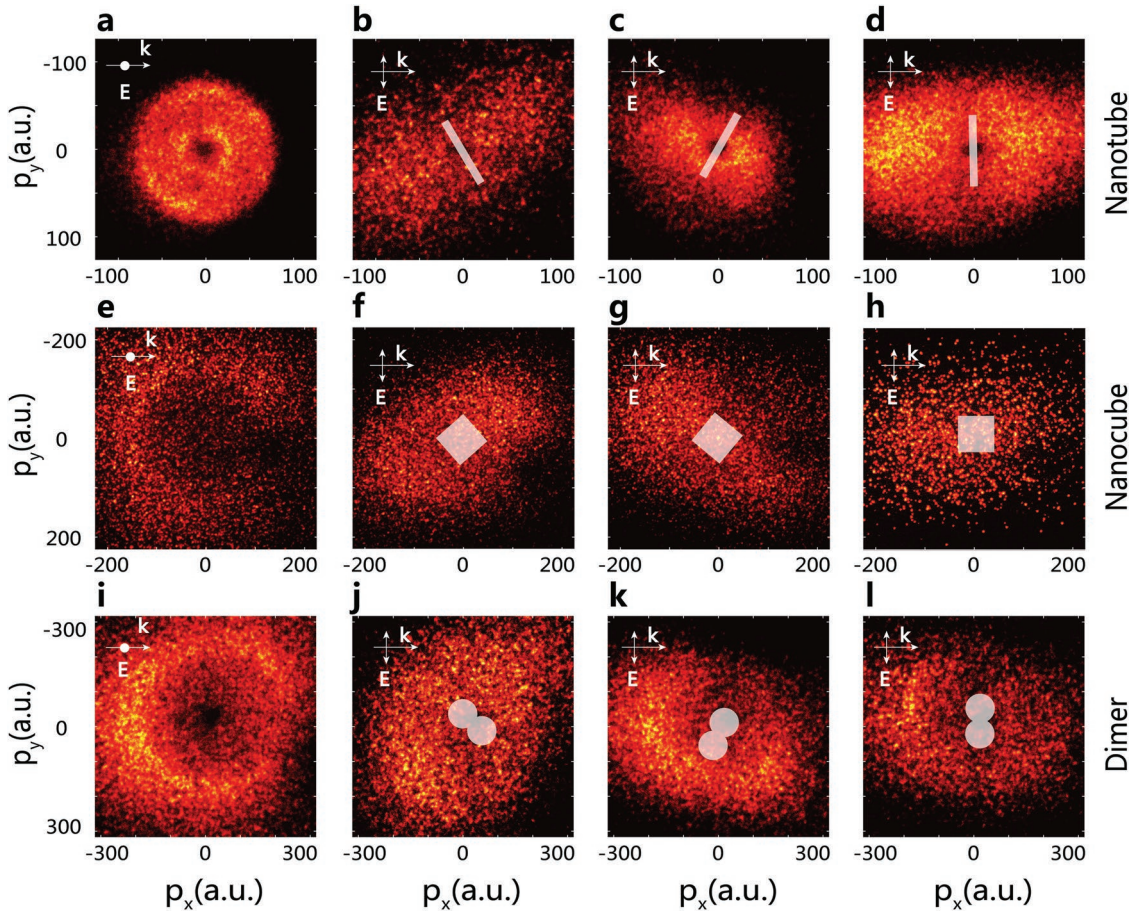

Figure 1. Display of the different repeatedly measured PIADs from different nanostructures. a) The round PIAD and the b–d) bandlike PIADs in the detector plane (*x*-*y* plane) from the nanotube. e) The ringlike PIAD and the f–h) bandlike PIADs from the NaCl nanocube. i) The ringlike PIAD and the j–l) bandlike PIAD from the Cu dimer. For all of the measurements, the laser propagates from the negative to the positive direction of the *x* axis. The laser polarization in each image is along the *y*-axis (double arrow) or perpendicular to the *x*-*y* plane (dot). The "hole structure," slight depression in ion yields, at the center and bottom right of the PIAD images are due to the degraded responsivity of our detector. Atomic units (a.u.) of the ion momentum are used. The white regions represent the differently oriented nanostructures.

Information for details). Ellipticity less than 0.5 is classified as round, which corresponds to that the orientation of the nanotube is perpendicular or only deviated from perpendicular by a small angle with respect to the detector plane. Ellipticity greater than 0.5 is classified as bandlike, which corresponds to that the orientation of the nanotube is parallel or only deviated from parallel by a small angle with respect to the detector plane. It is also noticed that the number of each specific PIAD tends to be different. The differently oriented nanotubes are supposed to be transmitted into the laser focus by the used ADL with equal opportunities (see Section S5, Supporting Information for details). However, different quantities of them get excited. By introducing a normalized ratio between the number of the specific PIAD and the number of all detected PIADs, we define the probability of the specific PIAD to quantify the excitation probability of correspondingly oriented nanostructures (**Figure 5**). For each group of the probability distribution, ≈100 frames of the PIAD images are recorded to ensure statistical credibility.

For example, when the polarization of the laser is perpendicular to the detector, the higher probability of the round PIAD (over 80%) is predominant compared with the rare bandlike PIADs (Figure 5a) from the nanotubes. The nanotube perpendicular to the detector is more likely to be excited than the nanotube parallel to the detector. The field strength inside the nanotube (Figure 2a,b) sensitively responds to the nanotube's orientation, explaining their orientation-dependent excitation probability. The field strength inside the nanotube parallel to the laser polarization shows a ≈30% enhancement at the focusing hotspot over the incident field (Figure 2a). In contrast, inside the nanotube perpendicular to the laser polarization, the suppressive field strength reveals a ≈30% reduction compared to the incident laser (Figure 2b). The ability to enhance the incident laser makes the nanotubes parallel to the polarization more likely to be excited, explaining the higher probability of the round PIADs.

Orientation discrimination provides a direct way to characterize the photoion emissions from the differently oriented nanostructures. Therefore, we can further introduce geometry, polarization, and concentration to control the photoion emission from the differently oriented nanostructures, which is the focus of this work. We prepare aerosolized nanostructures with different geometries like face-centered cubic NaCl crystals and

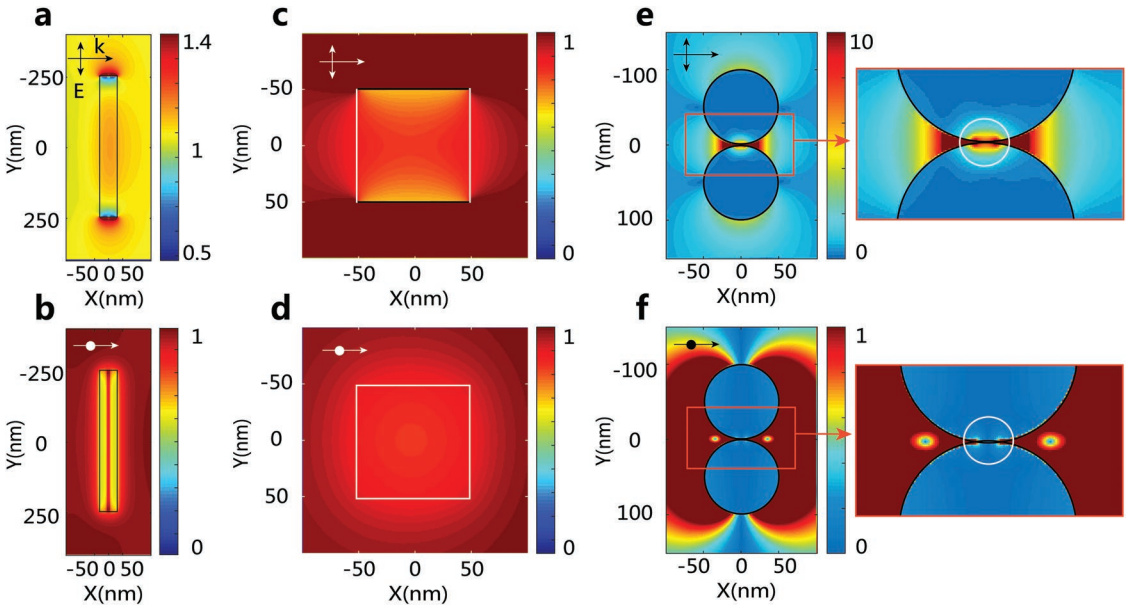

Figure 2. The field distribution of the nanostructures with different geometries by FDTD simulations. a) The field distribution of the multi-walled nanotube (length l = 500 nm and width r = 60 nm with a central 10 nm gap) when the laser polarization is along the y-axis (double arrow) or b) perpendicular to the x-y plane (dot). c) The field distribution of the nanocube (100 nm) when the laser polarization is parallel (along the y-axis) or d) perpendicular to the x-y plane. e) The field distribution of the dimer system (connected two Cu nanospheres) when the laser polarization is along the y-axis or f) perpendicular to the x-y plane. The color scale of the field intensities are normalized to the incident field intensity. The black lines represent the surface of different geometries. The nanotube and dimer are fixed along the y-axis. The orange box is the partial magnification of the field distribution near the connecting region.

Cu dimers, in addition to the carbon nanotubes (see Section S6, Supporting Information for more details of the sample characterization). Their specific PIADs (Figure 1) and the probabilities of PIADs (Figure 5) will be measured respectively before and after changing the laser polarization or the sample concentration. Similar to the nanotubes, we also manually divide the detected PIADs from the nanocubes and dimers into ringlike PIAD or bandlike PIAD. Relying on the correspondence between the shapes of the PIADs and the orientations of nanostructures (Figure 3), we can identify the orientations of the nanostructures (Figure 4) through the detected PIADs. The characteristics of the PIADs and the probabilities can be explained by the laser field distribution inside them in Figure 2 (see Section S7, Supporting Information for FDTD simulation details).

3. Controlling the Photoion Emission

3.1. Selective Excitation of the Nanotube by Laser Polarization

Firstly, we demonstrate how laser polarization affects the photoion emission from the differently oriented nanotubes. After rotating the laser polarization from perpendicular (along the z-axis in **Figure 6**c) to parallel (along the y-axis in Figure 6c) with respect to the detector, the probabilities of the round and bandlike PIADs show opposite trends (Figure 5a,b). The probability of the bandlike PIADs is increased from 17% to 71%, while the probability of the round PIADs reduces from 83% to 29%. More (less) nanotubes parallel (perpendicular) to the detector get excited, agreeing that the nanotube parallel to the laser polarization is always more likely to be excited. The selectively excited nanotube controlled by the polarization builds a directionally tunable nanoanode.

3.2. Geometry-Controlled Photoion Emission

To understand how the geometry affects the photoion emission, we have prepared more nanostructures with different geometries to compare with the nanotubes. Due to the face-centered cubic lattice structure, the crystallized NaCl crystals are generally cube-shaped.[29,30] Using the collision-type commercial atomizer (TSI, Model 3076), the micron-sized droplets are sprayed from the aqueous NaCl solution (from Aladdin) with a concentration of 3 g L^{-1}. After drying, the aerosolized NaCl nanocubes with a size of around 100 nm (see Section S2, Supporting Information for details) are generated. Then the nanocubes are respectively irradiated by the laser with the polarization parallel or perpendicular to the detector plane. The specific PIADs (Figure 1e–h) and probabilities of the PIADs (Figure 5c,d) from those nanocubes are recorded, showing two differences compared with the nanotubes.

The first difference focuses on the "hollow" ringlike PIAD of the nanocube (Figure 1e) compared with the round PIAD of the nanotube (Figure 1a), indicating the absence of low-energy ions from the nanocube. The second difference appears in the degraded orientation dependence of the shapes of the PIADs from the nanocubes compared with the highly orientation-dependent PIAD shapes from the nanotubes. When the laser polarization is perpendicular (parallel) to the detector, only the ringlike (bandlike) PIADs are observed regardless of the

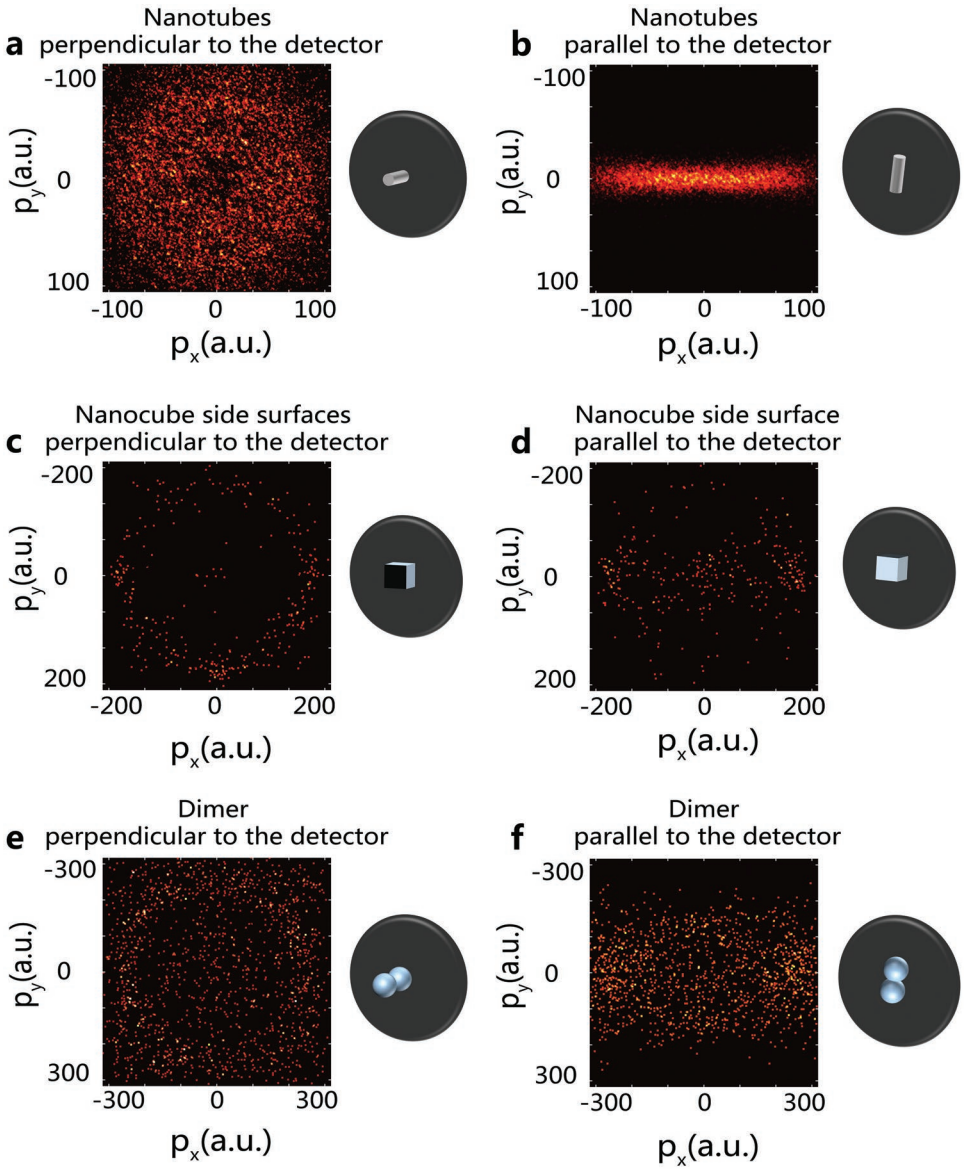

Figure 3. The simulated PIADs from differently oriented nanostructures simulated by the MD simulation. a,b) The simulated PIADs from the nanotubes perpendicular and parallel to the detector. c,d) The simulated PIADs from the nanocubes whose side surfaces perpendicular and parallel to the detector. e,f) The simulated PIADs from the dimers perpendicular and parallel to the detector. The schematic on the right of each PIAD image is the nanostructures with different orientations, where the black plate represents the fixed detector.

orientations of the nanocubes, supported by the 100% probability of the corresponding PIADs in Figure 5c,d.

To explain the above differences, we examine the field distributions (Figure 2c,d) inside the 100 nm nanocubes in the 800 nm laser. Firstly, the forward–backward symmetrical field distribution inside the nanocube without the focusing effects results from its smaller size than the laser wavelength. And the regions of the highest intensity (hotspots) of the internal field are always located at the shallow layer inside the nanocube close to the surfaces marked by the white color (defined as the side surfaces). And the field strength is gradually weakened from the surface to the deeper layer. At the shallow layer around each side surface, the identical field distribution (Figure 2d) equally induces the nanoplasma generation. The Coulomb interaction will immediately repel the generated photoions within the shallow layer around the side surfaces, and therefore show a "hollow" distribution with the absence of the low-energy ions. By the MD simulation, we simulate the ion emission from the nanocube. The nanocube whose side surfaces are perpendicular to the detector shows a "hollow" ringlike simulated PIAD (Figure 3c). It indicates that the ions are emitted from the side surfaces equally and supports the absence of the low-energy ions, while the nanocube whose side surfaces are parallel to the detector shows a bandlike simulated PIAD (Figure 3d). By the correspondence between the shapes of the PIADs and the orientations of the side surfaces, we can identify the orientations of the side surfaces of the nanocube through the detected PIAD (Figure 4c,d). Correspondingly, the hotspots inside the nanotube

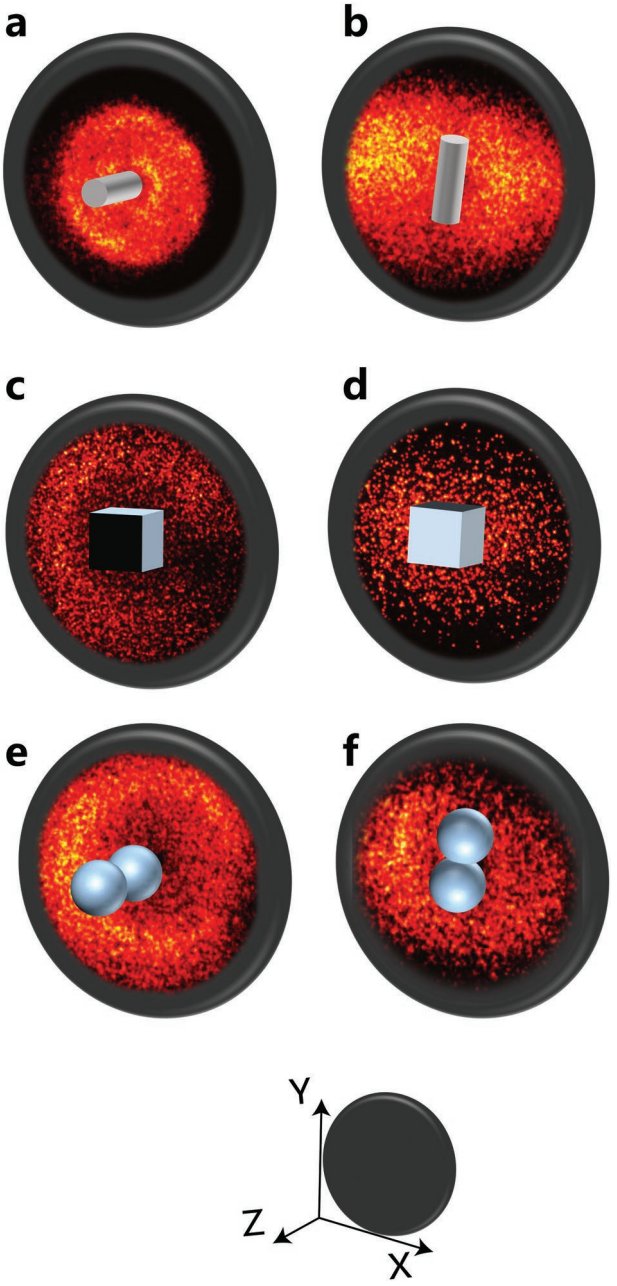

Figure 4. Identifying the orientations of the nanostructures by detected PIADs. a) The round PIAD originates from the nanotube perpendicular to the detector (along the *z*-axis in the lab coordinate). b) The bandlike PIAD originates from the nanotube parallel to the detector (along the *y*-axis in the lab coordinate). c) The round PIAD originates from the nanocube whose side surfaces (marked by white color) are perpendicular to the detector. d) The bandlike PIAD originates from the nanocube whose side surfaces (white surfaces) are parallel to the detector. e) The round PIAD originates from the dimer system perpendicular to the detector. f) The bandlike PIAD originates from the dimer system parallel to the detector. The detector is fixed in the *x*-*y* plane.

are always at the deeper layer in the bulk (Figure 2a,b). The ions generated inside the nanotube will experience different degrees of collision and scattering before they get sprayed, which averages the ion speeds. The slow ions fill the hollow regions. For this reason, we can observe a broad momentum distribution in both the experimental and simulated PIAD images of the nanotube (Figures 1a and 3a).

To explain the degraded orientation dependence for NaCl nanocubes, we show the field distributions inside the NaCl nanocubes with different orientations in Figure S1 (Supporting Information). Due to the face-centered cubic morphology, the NaCl crystals have a high rotational symmetry. So the location of the internal field hotspot is insensitive to the orientation of the NaCl crystals but only determined by the direction of the laser polarization. The hotspots are always located at the shallow layer close to the side surfaces that are parallel to the laser polarization in Figure 2c,d. So the localized plasma generation on the nanocubes is insensitive to the orientation, causing the orientation-independent PIADs. Moreover, the shape of the PIADs from the nanocubes can be switched between ringlike and bandlike by only changing the laser polarization. As shown in Figure 5c,d, before and after changing the laser polarization, the probability of the ringlike PIADs reduces from 100% to 0%, while the probability of the ringlike PIADs increases from 0% to 100%, both having a modulation depth of 100%. If we analogize the two specific PIADs to a traditional electrical sensor's high and low electrical levels, the nanocube can serve as an efficient optical polarization sensor. The advantage of the sensor based on the aerosolized nanocube is that it can be delivered in the gas or biological environment compared with the on-chip sensor.[31]

The insensitive ringlike PIADs from the Cu nanospheres (100 nm, from Chaowei Nanotechnology, aerosolized from the Cu nanosphere suspension with a concentration of 1 g L^{-1}) without orientation or polarization effect provide further evidence for the geometry-controlled photoion emission (see Figure S2, Supporting Information for details). The nanospheres are well-known for enhancing the laser field to show dipolar hotspots along with the polarization on the surface.[22] However, the field inside the Cu nanosphere always shows a shadowing distribution regardless of the laser polarization (Figure S2c,d, Supporting Information). The field strength is gradually weakened from the surface to the deeper layer. So the localized plasma is primarily generated over the shallow layer of the nanosphere, spraying the ions in all directions, which results in the constant ringlike PIADs.

3.3. Concentration-Controlled Photoion Emission from Mixed Aerosols

However, when increasing the concentration (to 3 g L^{-1}) of the Cu nanospheres suspension, we also observe bandlike PIADs in addition to the ringlike PIADs, as shown in Figure 1i–l. The bandlike PIAD is supposed to originate from the photoion emission from the aggregated clusters.[26] In the evaporation step of aerosolizing the Cu nanospheres, the undried droplets having 1, 2, 3, or more nanospheres respectively result in the formation of single nanospheres, dimers, trimers, or larger species. With a concentration of 3 g L^{-1}, the average number of the Cu nanosphere in each undried droplet is slightly less than one (see Section S2, Supporting Information for details). Some droplets still have a chance to contain two or more nanospheres and generate aggregated dimers. However, the used ADL can

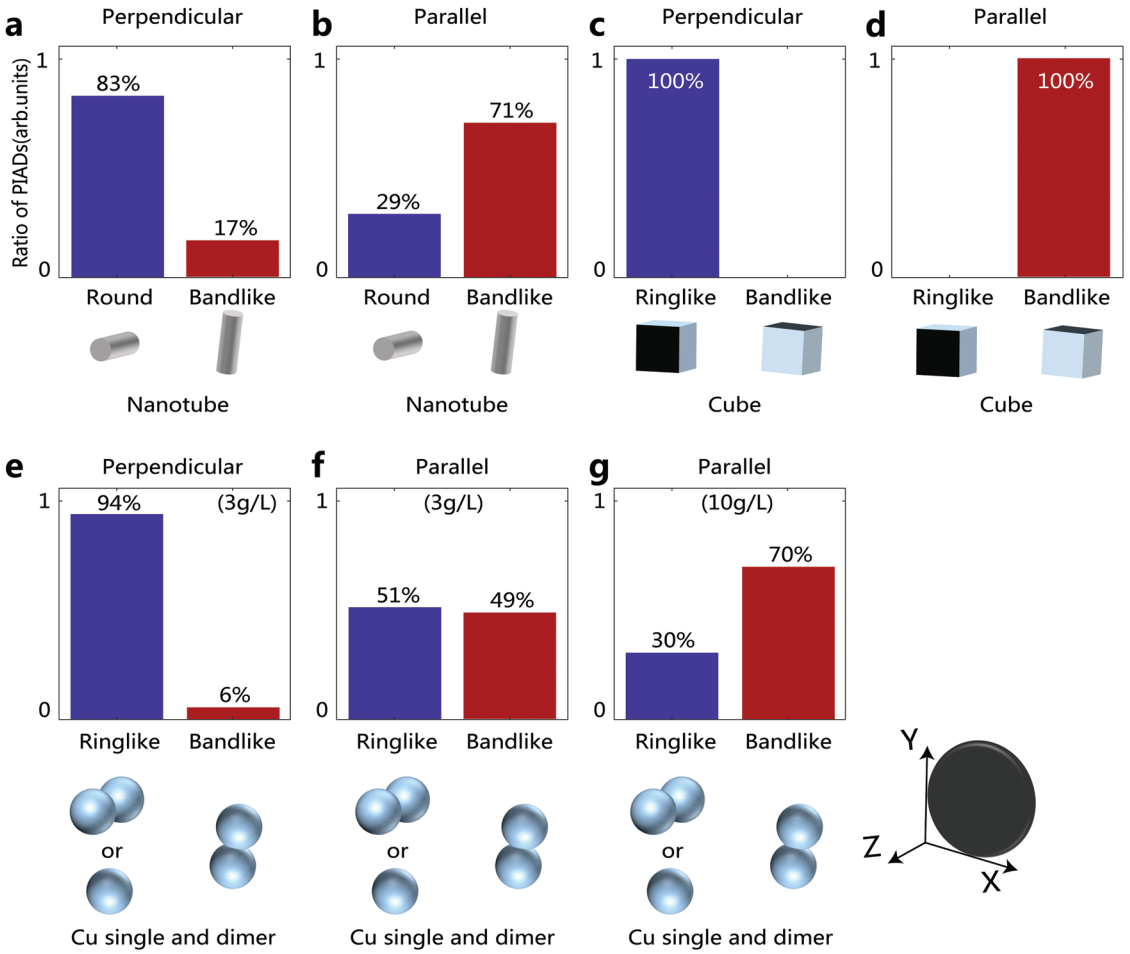

Figure 5. The probabilities of specific PIADs. a,b) The probabilities of the round PIAD and the bandlike PIAD from the nanotube. c,d) The probabilities of the ringlike PIAD and the bandlike PIAD from the nanocube. e,f) The probabilities of the ringlike PIAD and the bandlike PIAD from the mixed aerosols (Cu dimers and single Cu nanospheres) with a concentration of 3 g L^{-1}. g) The probabilities of the ringlike PIAD and bandlike PIAD from the mixed aerosols with a higher concentration of 10 g L^{-1}. The parallel/perpendicular above the ratio histogram shows whether the polarization of incident laser is parallel (along *y*-axis) or perpendicular (along *z*-axis) to the detector (fixed in the *x*-*y* plane). The diagram below the ratio histogram is the schematic to show the origin of the specific PIADs.

only transmit the single Cu nanosphere (100 nm) and dimer system (200 nm) (see Section S5, Supporting Information). The transfer of the trimers or larger species is strongly suppressed. Only the contributions of the single Cu nanospheres and the dimer systems to the observed PIADs need to be considered.

The Cu dimer system has been reported to show a donut-shaped 3D photoion emission.[26] The internal field inside the dimer system is only strongly enhanced around the connecting area between the two nanospheres to generate photoions (Figure 2e,f). We also simulate the ion emission from the differently oriented dimers by the MD simulation. The dimer whose axis is perpendicular (parallel) to the detector shows a ringlike (bandlike) simulated PIAD in Figure 3e,f. It indicates that the photoion emission is confined within the small angle between two nanospheres, which explains the donut-shaped 3D ion emission from the dimer. Similarly, the orientations of dimers should have been identified by the detected PIADs (Figure 4e,f). However, the ringlike PIAD may originate from the single nanospheres or the dimer systems perpendicular to the detector, making it difficult to retrace its origin. Correspondingly, the bandlike PIADs only originate from the dimer parallel to the detector.

Similar to the nanotube, the differently oriented dimer system can also be selectively excited by controlling the laser polarization. After changing the laser polarization, the probability of the bandlike PIADs is increased from 6% to 49%, while the probability of the ringlike PIADs reduces from 94% to 51% (Figure 5e,f). As we already demonstrated, the single nanospheres show polarization-independent ringlike PIADs. So the reduced probability of the ringlike PIAD only results from the suppressed excitation of the dimers, whose axes are perpendicular to the detector. In contrast, the increased probability of the bandlike PIAD indicates the increasing excitation of the dimers perpendicular to the detector. The dimer systems parallel to the polarization are also more likely to be excited, explained by the more substantial enhancement of their internal field (≈10.5 times the incident laser), shown in Figure 2e.

Considering that the bandlike PIAD only originates from the dimer parallel to the detector, its probability sensitively responds to the proportion of dimers in the mixed aerosols,

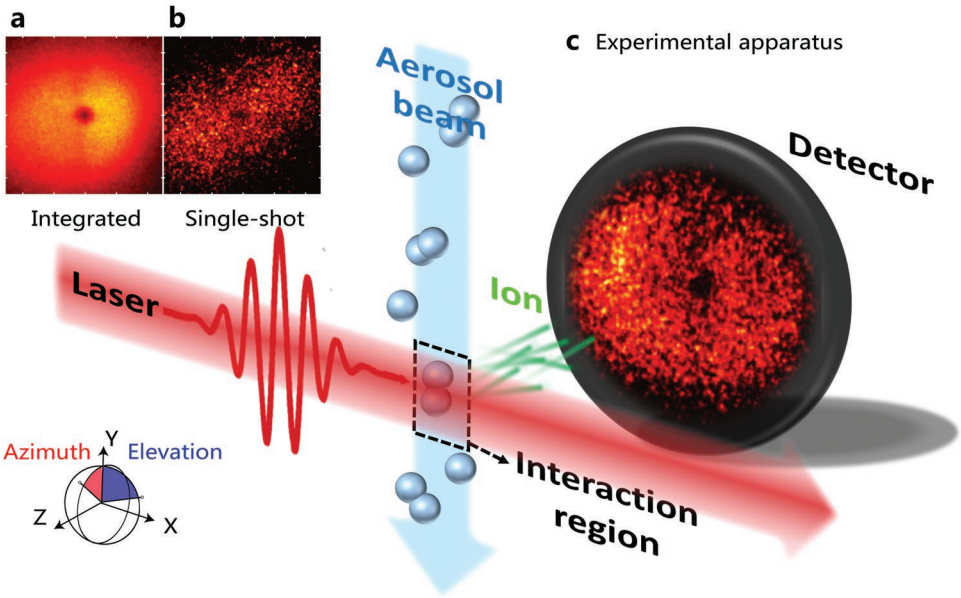

Figure 6. Experimental apparatus for observing single-shot photoion angular distribution from randomly oriented nanostructure. a,b) The integrated and the single-shot photoion angular distributions. c) The experimental apparatus where an 800-nm femtosecond laser pulse hits gas-carried aerosol nanostructures (dimers for example) transported by an aerodynamic lens and the emitted ions get recorded by a microchannel plate (MCP) and phosphor screen detector. The laser is propagating forward along the *x*-axis, while the detector is placed in the *x*-*y* plane. The azimuth angle and the elevation angle in the space coordinate are respectively shown by the red and blue region.

which can be controlled by the sample concentration. When increasing the concentration of Cu nanosphere suspension (from 3 to 10 g L^{-1}), the average number of Cu nanosphere in each undried droplet reaches nearly two, highly increasing the potential of assembling dimers. The increased proportion of the aggregated dimer systems in the mixed aerosols leads to the surging probability (from 49% to 70%) of the bandlike PIAD in Figure 5g compared to Figure 5f.

4. Conclusion

In conclusion, we establish a new orientation-binned scheme to identify the orientation of the complicated nanostructures by the detected PIADs. This unique capability is based on the PIAD and the orientation correlation. The orientation-dependent photoion emission can be characterized from two perspectives of PIADs and probabilities. We further show how to control the photoion emission of the differently oriented nanostructures by geometry, polarization, and concentration. It suggests new applications of photoion emission like directionally tunable nanoanode and optical sensors. Although not explicitly addressed in the text, access to characterize the photoion emission from differently oriented nanostructures opens up enormous possibilities for observing the time-resolved ionization dynamics of differently oriented complicated nanostructures by further combining with the pump–probe methods.

5. Experimental Section

Experimental Apparatus: The schematic illustration of the experimental apparatus is shown in Figure 6. In detail, the isolated nanostructures are firstly dispersed in pure water, which is next aerosolized by a commercial atomizer (TSI, Model 3076) to generate an aerosol beam consisting of the nanostructures suspended in the CO_2 carrier gas. Then the dried aerosol beam by a dryer will flow into the ADL system, which disperses the CO_2 carrier gas and collimates the samples along with the skimmer into the interaction region of the velocity-map imaging spectrometer where the pressure is $\approx 10^{-5}$ mbar. The ADL with a wider transmission window is used for maintaining a high transmission efficiency for different-sized nanostructures (detail in Figure S5, Supporting Information). The nanostructures with different orientations or geometries can be transmitted without obvious suppression. Then the nanostructures will be irradiated by femtosecond laser pulses at central wavelengths of 800 nm from a 1 kHz Ti: sapphire laser system. The irradiated nanostructures in the laser focus continuously get renewed, orient in random directions, and experience different irradiated intensities. The emitted cations from the irradiated nanostructures will be accelerated by an electrostatic field within the VMI lens system and collected on an MCP/phosphor screen detector, whose PIADs are then recorded by a charge-coupled device camera with a high readout frequency.[32]

Sing-Shot Imaging: When the laser pulse hits the nanostructure, the PIAD image with a higher ion yield can be effectively distinguished from the background image. The ion yield per shot of the background image is less than 10 counts, where the used laser intensities ($\approx 10^{13}$ W cm^{-2}) were too weak to cause the intense ionization of the background gases. In addition, the adjusting suspension concentration ensures the thin density (less than 10^5 particles cm^{-3}) of the aerosol sample in the interaction region, so the hit event always occurs within 0.1–1% rate even using the high-repetition-rate laser pulse (1 kHz).[24] And the low enough hit rate eradicates the probability that two or more samples simultaneously get hit by the laser pulses during one camera exposure (250 Hz).[33] Each frame of the PIAD image is entirely dominated by the single-shot excitation of only one sample (Figure 6b).

Sampling of Laser Intensity: The intensity-dependent pondermotive energy shift of the above-threshold ionization photoelectrons from atomic Argon gas to calibrate the accurate peak intensity of the laser fields in the reaction region is detected. The estimated peak laser intensity within the laser focus volume is 3.3×10^{13} W cm^{-2} for the

800-nm wavelength. It is noticed that even while keeping the constant peak intensity of the incident laser, the actual intensities irradiated on different nanostructures will span several orders of magnitude (from 6.6×10^{11} to 3.3×10^{13} W cm^{-2} for 800-nm wavelength), which sensitively depends on their positions within the laser focus. Only the nanostructures located at the center of the laser focus experience peak intensity. To avoid the laser focusing volume effect, the yield of the photofragments is employed to guide the actual irradiated intensity of each single-shot PIAD image. Selecting the PIAD images with similar ion yields ensures the constant irradiated intensity of the studied nanostructures. When the irradiated intensity is high enough to form the uniform plasma throughout the completely damaged sample, the intense collision averages the PIAD to be isotropous, degrading its sensitivity to the orientation of the nanostructure.[19,26] So, the PIAD images that primarily originate from the localized plasma generated from the ionization of the sample itself under moderate irradiated intensity is preferred to select. The different plasma generated in the Cu nanospheres can be easily distinguished by comparing the asymmetries between the PIADs and the field distributions (see Figure S3, Supporting Information for details). And the ion yields of the localized plasma on different materials show no significant difference in magnitude.[24] The ion yield ($\approx 10^3$ counts) of the localized plasma on the Cu nanosphere provides a general criterion for selecting the PIAD (Figure 6b) of the localized plasma on the nonspherical nanostructures with other materials. The ion yield was used ($\approx 10^3$ counts) for the subsequent PIAD selection in the text.

Supporting Information

Supporting Information is available from the Wiley Online Library or from the author.

Acknowledgements

X.H., H.H., and X.H. contributed equally to this work. Thanks engineer J. Su in the Center of Optoelectronic Micro&Nano Fabrication and Characterizing Facility, Wuhan National Laboratory for Optoelectronics of Huazhong University of Science and Technology for the support in the SEM test. The computation is completed in the HPC Platform of Huazhong University of Science and Technology. This work was supported by the National Natural Science Foundation of China (NSFC) (Grant Nos. 11934006, 92150106, 12021004, 11627809) and supported by the Innovation Project of Optics Valley Laboratory (OVL2021ZD001).

Conflict of Interest

The authors declare no conflict of interest.

Data Availability Statement

The data that support the findings of this study are available from the corresponding author upon reasonable request.

Keywords

aerosolized nanostructures, finite-difference time-domain, localized plasma, ultrafast lasers, velocity map imaging

Received: May 31, 2022
Revised: November 3, 2022
Published online: December 1, 2022

[1] S. Zherebtsov, T. Fennel, J. Plenge, E. Antonsson, I. Znakovskaya, A. Wirth, O. Herrwerth, F. Sussmann, C. Peltz, I. Ahmad, S. A. Trushin, V. Pervak, S. Karsch, M. J. J. Vrakking, B. Langer, C. Graf, M. I. Stockman, F. Krausz, E. Ruhl, M. F. Kling, *Nat. Phys.* **2011**, *7*, 656.
[2] J. Pettine, A. Grubisic, D. J. Nesbitt, *J. Phys. Chem. C* **2018**, *122*, 14805.
[3] J. Pettine, P. Choo, F. Medeghini, T. W. Odom, D. J. Nesbitt, *Nat. Commun.* **2020**, *11*, 1367.
[4] A. Grubisic, S. Mukherjee, N. Halas, D. J. Nesbitt, *J. Phys. Chem. C* **2013**, *117*, 22545.
[5] C. Hrelescu, T. K. Sau, A. L. Rogach, F. Jackel, G. Laurent, L. Douillard, F. Charra, *Nano Lett.* **2011**, *11*, 402.
[6] M. Lehr, B. Foerster, M. Schmitt, K. Kruger, C. Sonnichsen, G. Schonhense, H.-J. Elmers, *Nano Lett.* **2017**, *17*, 6606.
[7] K. R. Wilson, S. L. Zou, J. N. Shu, E. Ruhl, S. R. Leone, G. C. Schatz, M. Ahmed, *Nano Lett.* **2007**, *7*, 2014.
[8] R. Lachaine, E. Boulais, M. Meunier, *ACS Photonics* **2014**, *1*, 331.
[9] é. Boulais, R. Lachaine, M. Meunier, *Nano Lett.* **2012**, *12*, 4763.
[10] F. Dollar, T. Matsuoka, G. M. Petrov, A. G. R. Thomas, K. Krushelnick, *Phys. Rev. Lett.* **2011**, *107*, 065003.
[11] K. Furusawa, K. Takahashi, S. H. Cho, H. Kumagai, K. Midorikawa, M. Obara, *J. Appl. Phys.* **2000**, *87*, 1604.
[12] O. Kostya, *Plasma Phys. Controlled Fusion* **2018**, *61*, 014028.
[13] H. Huang, L. V. Zhigilei, *J. Phys. Chem. C* **2021**, *125*, 13413.
[14] H. Huang, Y. J. Xu, G. F. Luo, Z. B. Xie, W. Y. Ming, *Nanomaterials* **2022**, *12*, 1524.
[15] B. C. Stuart, M. D. Feit, S. Herman, A. M. Rubenchik, B. W. Shore, M. D. Perry, *J. Opt. Soc. Am. B* **1996**, *13*, 459.
[16] E. G. Gamaly, A. V. Rode, B. Luther-Davies, V. T. Tikhonchuk, *Phys. Plasmas* **2002**, *9*, 949.
[17] X. Wang, P. H. McMurry, *Aerosol Sci. Technol.* **2006**, *40*, 320.
[18] P. S. K. Liu, R. Deng, K. A. Smith, L. R. Williams, J. T. Jayne, M. R. Canagaratna, K. Moore, T. B. Onasch, D. R. Worsnop, T. Deshler, *Aerosol Sci. Technol.* **2007**, *41*, 721.
[19] D. D. Hickstein, F. Dollar, J. A. Gaffney, M. E. Foord, G. M. Petrov, *Phys. Rev. Lett.* **2013**, *112*, 313.
[20] J. A. Powell, A. M. Summers, Q. Liu, S. J. Robatjazi, P. Rupp, J. Stierle, C. A. Trallero-Herrero, M. F. Kling, A. Rudenko, *Opt. Express* **2019**, *27*, 27124.
[21] F. Suessmann, L. Seiffert, S. Zherebtsov, V. Mondes, J. Stierle, M. Arbeiter, J. Plenge, P. Rupp, C. Peltz, A. Kessel, S. A. Trushin, B. Ahn, D. Kim, C. Graf, E. Ruehl, M. F. Kling, T. Fennel, *Nat. Commun.* **2015**, *6*, 7944.
[22] P. Rupp, C. Burger, N. G. Kling, M. Kübel, M. F. Kling, *Nat. Commun.* **2019**, *10*, 4655.
[23] R. Signorell, M. Goldmann, B. L. Yoder, A. Bodi, E. Chasovskikh, L. Lang, D. Luckhaus, *Chem. Phys. Lett.* **2016**, *658*, 1.
[24] D. D. Hickstein, F. Dollar, J. L. Ellis, K. J. Schnitzenbaumer, K. E. Keister, G. M. Petrov, C. Ding, B. B. Palm, J. A. Gaffney, M. E. Foord, *ACS Nano* **2014**, *8*, 8810.
[25] P. Rosenberger, P. Rupp, R. Ali, M. S. Alghabra, M. F. Kling, *ACS Photonics* **2020**, *7*, 1885.
[26] F. Sun, H. Li, S. Song, F. Chen, J. Wang, Q. Qu, C. Lu, H. Ni, B. Wu, H. Xu, J. Wu, *Nanophotonics* **2021**, *10*, 2651.
[27] K. R. Wilson, S. Zou, J. Shu, E. Rühl, S. R. Leone, G. C. Schatz, M. Ahmed, *Nano Lett.* **2015**, *7*, 2014.
[28] T. Ditmire, T. Donnelly, A. M. Rubenchik, R. W. Falcone, M. D. Perry, *Phys. Rev. A* **1996**, *53*, 3379.
[29] E. Antonsson, F. Gerke, L. Merkel, I. Halfpap, B. Langer, E. Rühl, *Phys. Chem. Chem. Phys.* **2019**, *21*, 12130.
[30] M. J. Berg, K. R. Wilson, C. M. Sorensen, A. Chakrabarti, M. Ahmed, *J. Quant. Spectrosc. Radiat. Transfer* **2012**, *113*, 259.

[31] J. N. Anker, W. P. Hall, O. Lyandres, N. C. Shah, J. Zhao, R. P. Van Duyne, *Nat. Mater.* **2008**, *7*, 442.
[32] A. T. J. B. Eppink, D. H. Parker, *Rev. Sci. Instrum.* **1998**, *68*, 3477.
[33] F. Sussmann, S. Zherebtsov, J. Plenge, N. G. Johnson, M. Kubel, A. M. Sayler, V. Mondes, C. Graf, E. Ruhl, G. G. Paulus, D. Schmischke, P. Swrschek, M. F. Kling, *Rev. Sci. Instrum.* **2011**, *82*, 093109.